Segment-Based Wall Treatment Model for Heat Transfer Rate in Smoothed Particle Hydrodynamics

Hyung-Jun Park[1], Jaekwang Kim[2], Hyojin Kim[3,*]

[1] *Platform Technology Research Center, LG Chem, 30, Magokjungang 10-ro, Gangseo-gu, Seoul 07796, South Korea*
[2] *Department of Mechanical and Design Engineering, Hongik University, Sejong 30016, Republic of Korea*
[3] *Center for Healthcare Robotics, Korea Institute of Science and Technology, Seoul 02792, Republic of Korea*

constlearner89@gmail.com, jk12@hongik.ac.kr, hjinkim@kist.re.kr
* Corresponding author

Abstract

In this study, a smoothed particle hydrodynamics (SPH) model that applies a segment-based boundary treatment is used to simulate natural convection. In a natural convection simulated using an SPH model, the wall boundary treatment is a major issue because accurate heat transfer from boundaries should be calculated. The boundary particle method, which models the boundary by placing multiple layers of particles on and behind the wall boundary, is the most widely used boundary treatment method. Although this method can impose accurate boundary conditions, boundary modeling for complex shapes is challenging and requires excessive computational costs depending on the boundary shape. In this study, we utilize a segment-based boundary treatment method to model the wall boundary and apply this method to the energy conservation equation for the wall heat transfer model. The proposed method solves the problems arising from the use of boundary particles and simultaneously provides accurate heat transfer calculation results for the wall. In various numerical examples, the proposed method is verified through a comparison with available experimental results, SPH results using the boundary particle method, and finite volume method (FVM) results.

Keywords: Smoothed particle hydrodynamics; SPH; natural convection; heat transfer; wall boundary treatment; boundary modeling

1   Introduction

Natural convection is heat transfer mechanism in which density variations of thermal fluids play a significant role in thermal transport. Natural convection in enclosed systems has been extensively researched owing to its numerous practical applications in various industrial and everyday scenarios, including airflow for a comfortable indoor environment, heat control in data centers through convection, and cooling systems for various industrial facilities [1, 2]. To analyze natural convection, grid-based numerical methods from a Eulerian perspective such as finite volume method (FVM) [3, 4] and finite element method (FEM) [5, 6, 7], are widely used in both industry and academia. However, these methods frequently require supplementary schemes to manage turbulent flows [8, 9], which can develop even under mild external conditions owing to the low-density fluid in natural convection scenarios. In contrast, smoothed particle hydrodynamics (SPH) has gained attention as a numerical analysis technique for simulating flows with interfaces [10, 11, 12]. One of the primary advantages of the SPH scheme when handling interface problems is its particle-based Lagrangian approach, which avoids the need for intricate constraints, such as maintaining high grid quality or grid connectivity, which are commonly required by grid-based methods [13, 14, 15]. Moreover, SPH excels in examining fluid dynamics involving free surfaces or multiple phases because interfaces can be easily tracked by the movement of particles. However, when simulating natural convection using SPH, there are still many areas for improvement, including accuracy issues related to boundary condition enforcement at wall boundaries, when compared to its counterparts [16].

Various formulations have been proposed to simulate natural convection using SPH. Cleary PW [17] applied SPH to energy equations and modeled natural convection based on the Boussinesq approximation. Szewc et al. [18] proposed an SPH model that implemented natural thermal conduction without the Boussinesq approximation. Building upon pioneering research, Yang and Kong [19] analyzed the behavior of natural convection based on the Rayleigh and Prandtl numbers using SPH. Ng et al. [20] evaluated two representative boundary particle methods for simulating the heat transfer at walls. Garoosi et al. [21] proposed a model for heat transfer analysis in fluid-structure interaction problems by applying a kernel derivative-free model to an incompressible SPH (ISPH). Furthermore, Yang et al. [22] conducted stable simulations of natural convection, even at high Rayleigh numbers, by combining four techniques primarily used for solution stabilization in SPH: kernel gradient correction, particle shifting technique, δ-SPH, and asymmetric pressure approximation. While these studies have contributed to enhancing the accuracy of solutions and proposing various models to simulate natural convection and implement the physical phenomena, they have not addressed the limitations associated with boundaries.

In SPH, when fluid particles approach a physical solid boundary, they encounter particle deficiency issues. This is known as the boundary truncation problem and is critical because the SPH scheme requires maintenance of a certain number of interacting particles to ensure the accuracy and stability of the solution [23, 24]. To address these issues in SPH, conventional treatment involves placing multiple layers of boundary particles. However, determining the appropriate positions for the boundary particles becomes a challenging task when dealing with complex bounday geometries. In addition, an increase in the number of boundary particles leads to a significant increase in the computational costs [25]. Hence, we aim to develop a new method that overcomes these limitations while accurately predicting the heat transfer across solid

boundaries.

On the other hand, there also exist various methods that do not rely on the use of boundary particles in SPH. The semi-analytical model proposed by Kulasegaram et al. [26] addresses the issue of boundary truncation by applying a normalization factor to the SPH formulation of the fluid particles approaching the boundary region. Ferrand et al. [27] proposed an extended unified semi-analytical model that could be applied to complex boundary shapes. Mayrhofer et al. [28] extended the unified semi-analytical model into three dimensions, wherea Kostorz and Esmail-Yakas [29] focused on precisely calculating the normalization factor in this model. More recently, Park et al. [30] introduced a segment-based boundary treatment method that employs line segments in two-dimensions (2D) and triangular segments for three-dimensions (3D) respectively, to model the wall boundary instead of boundary particles. The use of boundary segments efficiently addresses the particle deficiency at the boundaries, while enhancing the solution accuracy. Their formulation was primarily applied to the continuity and momentum conservation equations and was used to accurately calculate the physical quantities at the boundary.

In this study, by extending the work of Park et al. [30], we propose a wall boundary model for an energy conservation equation that considers heat transfer from the wall boundary. In the segment-based boundary treatment method, the boundary truncation problem is addressed by direct compensation of the truncated region through the addition of specific terms called *boundary truncation term* to the original equation. Whereas previous studies proposed formulations for the boundary truncation term but only for the pressure gradient and viscosity terms in a momentum conservation equation. However, we introduce a boundary truncation term for the energy equation, enabling the efficient calculation of heat transfer from wall boundaries composed of segments. The proposed method addresses issues related to boundary particles and simultaneously delivers precise calculations for heat transfer from the wall.

The rest of the paper is structured as follows: In Section 2, we briefly describe the governing equations for non-isothermal buoyant fluid flow. A formulation for the boundary truncated terms of the energy equation is proposed in Section 3. The details of the numerical methods are summarized in the same section. In Section 4, we validate our approach using the results from the experiment and FVM [31]. Furthermore, the computational performance of the proposed approach is compared with that of a conventional SPH scheme based on the boundary particle method. The main conclusions are summarized in Section 5.

2 Governing equations

In this section, we present the governing equations for simulating the non-isothermal buoyant fluid flow. These equations encompass the principles of mass, momentum, and energy conservations:

$$\frac{D\rho}{Dt} = -\rho \nabla \cdot \mathbf{v}, \tag{2.1}$$

$$\frac{D\mathbf{v}}{Dt} = -\frac{1}{\rho}\nabla p + \frac{\mu}{\rho}\nabla^2 \mathbf{v} + \mathbf{F}^B, \tag{2.2}$$

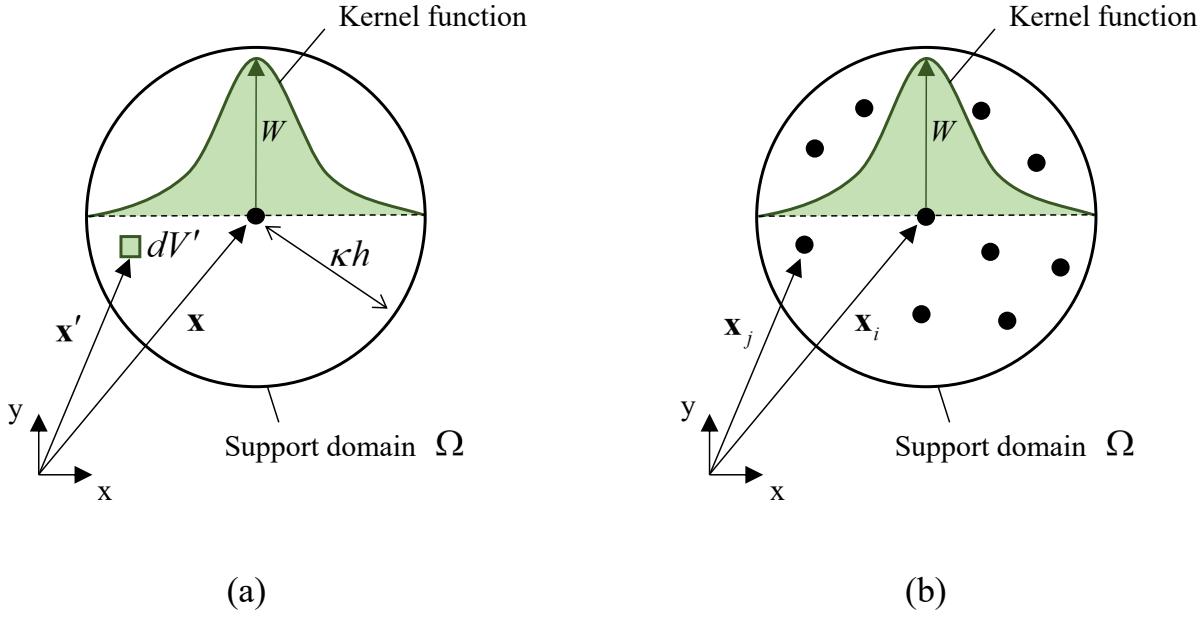$$\frac{DT}{Dt} = -\frac{k}{\rho C_p}\nabla^2 T, \tag{2.3}$$

3

Figure 1: Schematic configuration for SPH approximation: (a) kernel approximation and (b) particle approximation.

where ρ is fluid density, $\mathbf{v}$ is velocity, p is pressure, μ is fluid dynamic viscosity, $\mathbf{F}^B$ is buoyancy force, T is temperature, k is fluid thermal conductivity, C_p is fluid specific heat, and D/Dt denotes the material derivative.

In this study, the following Boussinesq approximation is used to model the buoyancy force $\mathbf{F}^B$ in Eq. (2.2):

$$\mathbf{F}^B = \mathbf{g}\beta(T - T_r), \tag{2.4}$$

in which $\mathbf{g}$ is the gravitational acceleration, β is the fluid thermal expansion coefficient, T_r is the reference temperature. When the fluid temperature is higher than the reference temperature T_r, the fluid experiences an upward buoyancy force.

The Boussinesq approximation is a model mainly used to simulate buoyancy-driven flows, and this approximation is used in this paper because of its ability to describe the buoyancy effect due to temperature with a simple term [32]. In other words, once the temperature field is determined using the energy conservation equation in (2.3), the buoyancy force associated with the temperature in the next step can be easily calculated.

3 Numerical modeling

This section presents a numerical method for discretizing the governing equations. In this sections, the SPH formulation process, which involves the discretization of the spatial domain using particles, is first introduced. Subsequently, the handling of the boundary conditions, wall heat transfer and viscous models, the particle shifting algorithm, and the integration scheme for the time domain are presented.

4

3.1 Weakly compressible SPH formulation

In the problem domain, the SPH method performs a discretization process in two steps. The first step is "kernel approximation", which employes a kernel function, and weight function based on distance, to approximate the field function $f(\mathbf{x})$, at position $\mathbf{x}$. Within the valid region of the kernel function, the value of $f(\mathbf{x})$ is approximated by integrating the product of the field function $f(\mathbf{x}')$ and the kernel function at position $\mathbf{x}'$ within the area. When the kernel approximation is applied to both $f(\mathbf{x})$ and its derivatives, the following equations are obtained:

$$f(\mathbf{x}) \cong \int_{\Omega} f(\mathbf{x}') W(\mathbf{x} - \mathbf{x}', h) \, dV', \tag{3.1}$$

$$\nabla f(\mathbf{x}) \cong -\int_{\Omega} f(\mathbf{x}') \nabla W(\mathbf{x} - \mathbf{x}', h) \, dV', \tag{3.2}$$

where W represents the kernel function, h is the smoothing length that defines the effective area of the kernel function, dV' is the small volume within the integrated area, and Ω is the support domain. As shown in Fig. 1(a), the radius of the support domain is determined using κh, where κ is a parameter dependent on the kernel function. We use the Wendland kernel function and in this case, κ is 2 [33].

In the second step "particle approximation", the integral regions of Eqs. (3.1) and (3.2) are discretized using a finite number of particles. After placing particle i at the target position $\mathbf{x}$ and particle j at position $\mathbf{x}'$ within the support domain, and substituting the infinitesimal volume dV' with the volume of particle j ($dV' \cong \Delta V_j = m_j / \rho_j$), we obtain the following discretized equations [34]:

$$f(\mathbf{x}_i) = \sum_{j=1}^{N} f(\mathbf{x}_j) W(\mathbf{x}_i - \mathbf{x}_j, h) \frac{m_j}{\rho_j}, \tag{3.3}$$

$$\nabla f(\mathbf{x}_i) = \sum_{j=1}^{N} f(\mathbf{x}_j) \nabla_i W(\mathbf{x}_i - \mathbf{x}_j, h) \frac{m_j}{\rho_j}, \tag{3.4}$$

in which m is the mass, $\nabla_i W$ is a derivative of the kernel function with respect to particle i, and the subscripts i and j refer to particles i and j, respectively, see Fig. 1(b).

By applying Eqs. (3.3) and (3.4) into the governing equations in Eqs. (2.1)-(2.3), the following SPH formula can be obtained [17]:

$$\frac{D\rho_i}{Dt} = \rho_i \sum_{j=1}^{N} \frac{m_j}{\rho_j} \mathbf{v}_{ij} \nabla_i W(\mathbf{x}_{ij}, h) + D_i, \tag{3.5}$$

$$\frac{D\mathbf{v}_i}{Dt} = -\sum_{j=1}^{N} m_j \left(\frac{p_i + p_j}{\rho_i \rho_j} \right) \nabla_i W(\mathbf{x}_{ij}, h) + \mathbf{F}_i^V + \mathbf{F}_i^B, \tag{3.6}$$

$$\frac{DT_i}{Dt} = -\frac{1}{\rho_i C_p} \sum_{j=1}^{N} \frac{m_j}{\rho_j} \left(\frac{k_i k_j}{k_i + k_j} \right) \frac{\mathbf{x}_{ij} \cdot \nabla_i W(\mathbf{x}_{ij}, h)}{|x_{ij}|^2} (T_i - T_j), \tag{3.7}$$

in which $\mathbf{v}_{ij}$ represents $\mathbf{v}_i - \mathbf{v}_j$, $\mathbf{x}_{ij}$ represents $\mathbf{x}_i - \mathbf{x}_j$, D_i indicates the diffusive term for the density

change, and $\mathbf{F}^V$ denotes the viscous force term.

The term D_i in Eq. (3.5) is an addition aimed at stabilizing the density field, and this numerical stabilization approach is referred to as the δ–SPH scheme. In this study, the following equation as proposed by Sun et al. [35] is used:

$$D_i = -2\delta h c \sum_{j=1}^{N} \frac{m_j}{\rho_j} \psi_{ij} \frac{\mathbf{x}_{ij} \cdot \nabla_i W(\mathbf{x}_{ij}, h)}{\mathbf{x}_{ij}^2} \quad \text{with} \quad \psi_{ij} = (\rho_j - \rho_i) - \frac{1}{2}\left(\langle \nabla \rho \rangle_j^L + \langle \nabla \rho \rangle_i^L\right) \cdot (\mathbf{r}_j - \mathbf{x}_i), \tag{3.8}$$

where δ is a parameter that determines the magnitude of density diffusion, c is the numerical speed of sound, and $\langle \nabla \rho \rangle_i^L$ and $\langle \nabla \rho \rangle_j^L$ denote re-normalized density gradient terms, as referred to in [36]. Here, δ is set to 0.1.

In Eq. (3.6), the physical viscosity term $\mathbf{F}^V$ is defined as [37]:

$$\mathbf{F}_i^V = \sum_{j=1}^{N} \frac{m_j(\mu_i + \mu_j)}{\rho_i \rho_j} \frac{\mathbf{x}_{ij} \cdot \nabla_i W(\mathbf{x}_{ij}, h)}{\mathbf{x}_{ij}^2 + (0.1h)^2} \mathbf{v}_{ij}. \tag{3.9}$$

In weakly compressible SPH (WCSPH), pressure is determined based on the change in density. In this study, the fluid pressure p is calculated using the following equation of state:

$$p_i = c^2(\rho_i - \rho_0), \tag{3.10}$$

in which ρ_0 represents the initial density of the fluid. The numerical sound speed c is assigned a value that satisfies $c > 10v_{\max}$ to impose a weak compressibility condition. $v_{\max}$ is the predicted maximum velocity value [20], determined by the problem.

3.2 Boundary treatment

Now, we employ the segment-based wall boundary treatment method introduced by Park et al. [30, 38]. In traditional SPH boundary treatment methods, multiple layers of particles, referred to as boundary particles, are placed at the boundary, as shown in Fig. 2. These particles serve to restore the support domain of particle i, which is truncated near the boundary. Various methodologies, such as the ghost particle method and mirror particle method [16, 39], exist depending on the placement of the boundary particles or updating of the physical values.

The segment-based boundary treatment method directly addresses the truncated region of the support domain without the placement of boundary particles, see Fig. 3. This approach offers several advantages, including avoiding the challenges associated with positioning multiple layers of boundary particles in complex shapes, greater computational efficiency compared with the boundary particle method, and preservation of the original grid shape created by computer aided design (CAD) tools. In other words, boundary modeling can be performed efficiently and easily using CAD tools.

In the segment boundary treatment method, the support domain is divided into the fluid domain Ω_f and the boundary domain Ω_b during the kernel approximation process (Fig. 4), and Eqs. (3.1) and (3.2) can be
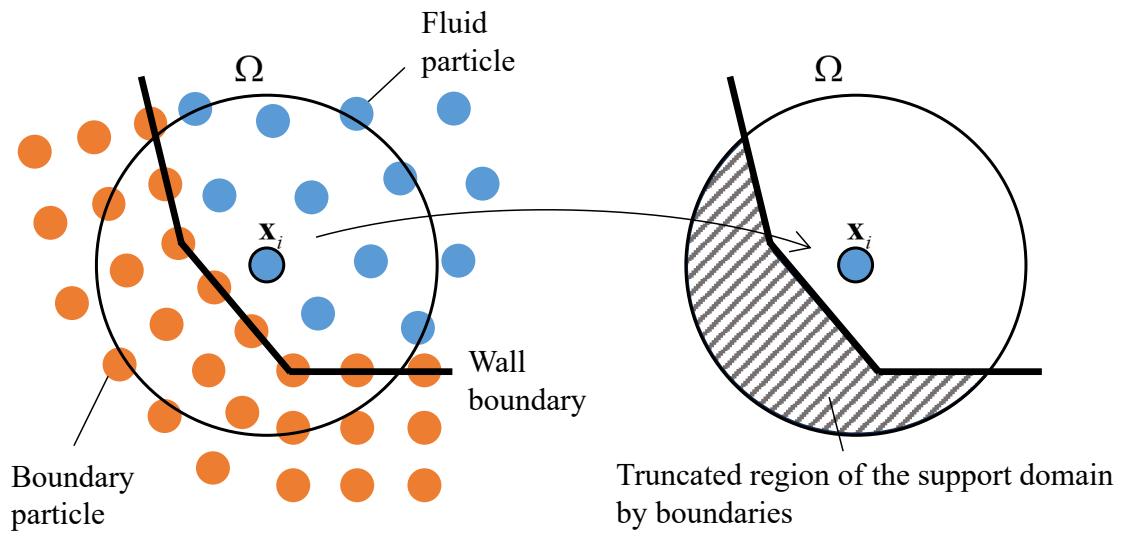
6

Figure 2: Arrangement of the three-layered boundary particles and region of the support domain of the particle i, truncated by boundaries.
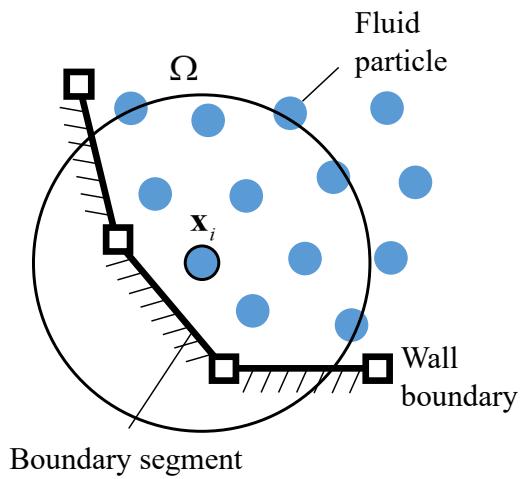

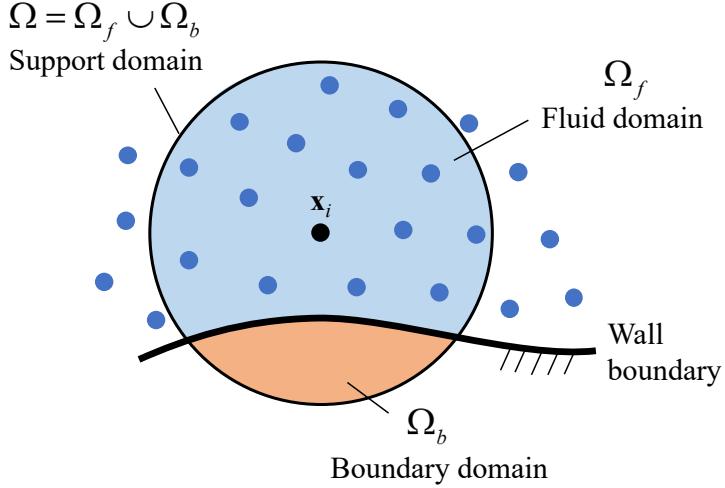**Figure 3:** Wall boundary modeling using segment-based boundary treatment method.

Figure 4: Support domain (Ω) divided into fluid (Ω_f) and boundary (Ω_b) domains.

expressed as follows [30, 38]:

$$f(\mathbf{x}) \cong \int_{\Omega_f} f(\mathbf{x}')W\,dV' + \int_{\Omega_b} f(\mathbf{x}')W\,dV', \tag{3.11}$$

$$\nabla f(\mathbf{x}) \cong -\left(\int_{\Omega_f} f(\mathbf{x}')\nabla W\,dV' + \int_{\Omega_b} f(\mathbf{x}')\nabla W\,dV' \right), \tag{3.12}$$

in which $W = W(\mathbf{x}_{ij}, h)$.

An examination of Eqs. (3.5)-(3.7) shows that these equations primarily comprise the differential terms for the kernel function. Therefore, we utilize only Eq. (3.12) to derive the equation for the boundary treatment. By formulating Eq. (3.12) in a symmetrical manner and incorporating several inter-domain correlations, following equation can be obtained [38]:

$$\nabla f(\mathbf{x}_i) = \frac{1}{\int_{\Omega_f} W\,dV'} \left(\int_{\Omega_f} \left(f(\mathbf{x}') - f(\mathbf{x}_i) \right) \nabla_i W\,dV' + \int_{\partial\Omega_b} \left(f(\mathbf{x}') - f(\mathbf{x}_i) \right) W\mathbf{n}\,dS' \right), \tag{3.13}$$

where $\partial\Omega_b$ means the cross section where the support domain of particle i is cut by the boundary, dS' is the microscopic area for that face, and $\mathbf{n}$ is a normal vector pointing outward from the face, see Fig. 5. Although the derivation process is different, Eq. (3.13) has the same form as that of a semi-analytical approach, and the denominator on the right hand side of Eq. (3.13) is called the re-normalization factor, and various studies have been presented to calculate it [25, 29].

In this study, the simplest approach used by Park and Seo [38] is adopted for the calculation of the re-normalization factor. when the particle approximation is applied soley to the fluid domain, including the
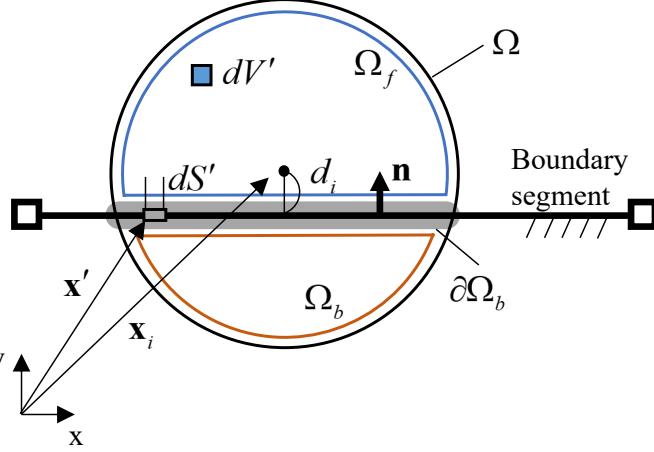
Figure 5: Geometric configuration for the segment-based boundary treatment method.

simplified renormalization factor, Eq. (3.13) can be expressed as follows:

$$\nabla f(\mathbf{x}_i) = \frac{1}{\sum\limits_{j=1}^{N} W \frac{m_j}{\rho_j}} \left(\sum_{j=1}^{N} (f(\mathbf{x}_j) - f(\mathbf{x}_i)) \nabla_i W \frac{m_j}{\rho_j} + \int_{\partial \Omega_b} (f(\mathbf{x}') - f(\mathbf{x}_i)) W \mathbf{n} dS' \right). \qquad (3.14)$$

The physical values at the boundary, expressed as $f(\mathbf{x}')$ in Eq. (3.14), include pressure $p(\mathbf{x}')$, velocity $\mathbf{v}(\mathbf{x}')$, and temperature $T(\mathbf{x}')$. For each boundary value, the following conditions are applied [38]:

- For pressure $p(\mathbf{x}')$

$$p(\mathbf{x}') = p_i + \frac{\rho_i}{2\Delta t}(\mathbf{v}_i - \mathbf{v}(\mathbf{x}')) \cdot (\mathbf{x}' - \mathbf{x}_i), \qquad (3.15)$$

- For velocity $\mathbf{v}(\mathbf{x}')$

$$\mathbf{v}(\mathbf{x}')_{\text{normal}} = \left(\frac{\kappa h}{d_i} \right) (\mathbf{v}_w \cdot \mathbf{n}) - \left(\frac{\kappa h}{d_i} - 1 \right) (\mathbf{v}_i \cdot \mathbf{n}), \qquad (3.16)$$

$$\mathbf{v}(\mathbf{x}')_{\text{tangent}} = \begin{cases} \mathbf{v}_i - (\mathbf{v}_i \cdot \mathbf{n})\mathbf{n} & \text{for the free} - \text{slip condition}, \\ -(\mathbf{v}_i - (\mathbf{v}_i \cdot \mathbf{n})\mathbf{n}) & \text{for the non} - \text{slip condition}, \end{cases} \qquad (3.17)$$

- For temperature $T(\mathbf{x}')$

$$T(\mathbf{x}') = T_w, \qquad (3.18)$$

in which Δt is the time step size, d_i is the distance from the particle i to the boundary plane, $\mathbf{v}(\mathbf{x}')_{normal}$ and $\mathbf{v}(\mathbf{x}')_{tangent}$ are the velocities in the normal and tangential directions to the wall, respectively, $\mathbf{v}_w$ is the wall velocity, and T_w is the wall temperature. Under adiabatic conditions, $T(\mathbf{x}') = T_i$, preventing heat transfer from the wall.

The last integral term on the right side of Eq. (3.14) is directly calculated using the Gaussian integration, and the calculation is performed using the integration algorithm proposed by Ref. [30].

9

3.3 Heat transfer rate and viscous force by wall boundary

The calculation of the heat transfer rate and viscous force of the wall require discretization involving the Laplacian operator, as shown in Eqs. (2.2) and (2.3). In this study, the Laplacian operator is discretized using Monaghan's approach [40]. The SPH formulation of the Laplacian operator for field functions $f(\mathbf{x}_i)$ and $g(\mathbf{x}_i)$ is as follows:

$$
\left(\frac{1}{\rho} \nabla \cdot f_i \nabla \right) g_i \cong \frac{1}{\sum_{j=1}^{N} W \frac{m_j}{\rho_j}} \left(\frac{1}{\rho_i} \sum_{j=1}^{N} (f_i + f_j) \left(\frac{g_i - g_j}{|\mathbf{x}_{ij}|^2} \right) (\mathbf{x}_{ij} \cdot \nabla_i W) \frac{m_j}{\rho_j} \right.
$$
$$
\left. + \frac{1}{\rho_i} \int_{\partial \Omega_b} (f_i + f') \left(\frac{g_i - g'}{|\mathbf{x}_i - \mathbf{x}'|^2} \right) ((\mathbf{x}_i - \mathbf{x}') \cdot \mathbf{n}) W dS' \right), \tag{3.19}
$$

where $f_i = f(\mathbf{x}_i)$, $g_i = g(\mathbf{x}_i)$, $f' = f(\mathbf{x}')$, and $g' = g(\mathbf{x}')$.

Applying the last term on the right-hand side of Eq. (3.19) into the viscosity term of Eq. (2.2), we obtain the following wall viscosity term $\mathbf{F}_i^{VW}$:

$$
\mathbf{F}_i^{VW} = \frac{1}{\rho_i \sum_{j=1}^{N} W \frac{m_j}{\rho_j}} \left(\int_{\partial \Omega_b} (\mu_i + \mu') \left(\frac{\mathbf{v}_i - \mathbf{v}'}{|\mathbf{x}_i - \mathbf{x}'|^2} \right) ((\mathbf{x}_i - \mathbf{x}') \cdot \mathbf{n}) W dS' \right), \tag{3.20}
$$

in which μ' is assigned the value of μ_i.

Similarly, applying the last term on the right-hand side of Eq. (3.19) to the energy conversion equation in Eq. (2.3) yields the wall heat transfer rate DT_i^W / Dt:

$$
\frac{DT_i^W}{Dt} = \frac{1}{\rho_i C_p \sum_{j=1}^{N} W \frac{m_j}{\rho_j}} \left(\int_{\partial \Omega_b} (k_i + k') \left(\frac{T_i - T'}{|\mathbf{x}_i - \mathbf{x}'|^2} \right) ((\mathbf{x}_i - \mathbf{x}') \cdot \mathbf{n}) W dS' \right), \tag{3.21}
$$

in which k' is assigned the value of k_i.

In Eq. (3.19), the arithmetic mean $(f_i + f')/2$ for the field function f can be replaced with the harmonic mean $2 f_i f' / (f_i + f')$ [33, 40].

3.4 Particle shifting algorithm

In the SPH simulations, local particle disordering can occur as the time step progresses. This disordering of particles causes a particle clustering phenomenon called tensile instability and yields non-physical analysis results [41]. To alleviate this disordering, the particle shifting technique (PST) is commonly used in the field of SPH. In this study, we use the approach proposed by Sun et al. [35] as follows:

$$
\delta r_i = -2(\Delta t) \left| \mathbf{v}_{\max} \right| (\kappa h) \sum_{j=1}^{N} \left[1 + R \left(\frac{W}{W(\Delta x)} \right)^n \right] \nabla_i W \frac{m_j}{(\rho_i + \rho_j)}, \tag{3.22}
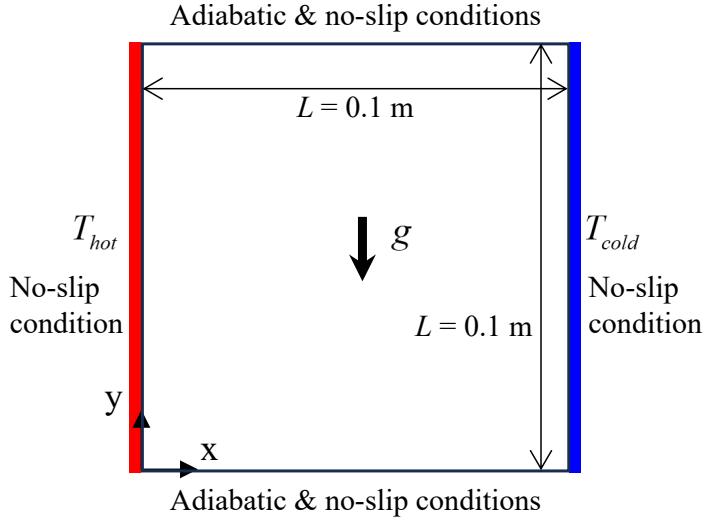$$

Figure 6: Domain description for natural convection in a square cavity problem.

where Δx represents the initial interparticle spacing, and R and n are problem-dependent values, which were set to 2 and 0.4, respectively, in this study.

Once the change in velocity at each time step is calculated using the momentum conservation equation, it cab be used to compute the velocity value for the next step. This, in turn, determines the position value for the next step. Eq. (3.22) is then added to the determined position value to alleviate the particle disorder.

Considering boundary truncation near the boundary, Eq. (3.22) can be written as [38]:

$$
\begin{aligned}
\delta r_i = -2(\Delta t)v_{\max}(\kappa h) \Bigg(&\sum_j^N \left[1 + R\left(\tfrac{W}{W(\Delta x)} \right)^n \right] \nabla_i W \tfrac{m_j}{(\rho_i + \rho_j)} \\
&+ \tfrac{1}{2} \int_{\Omega_b} \left[1 + R\left(\tfrac{W(\mathbf{x}_i - \mathbf{x}')}{W(\Delta x)} \right)^n \right] \nabla_i W \, dV' \Bigg)
\end{aligned}
\tag{3.23}
$$

3.5 Time integration scheme

In SPH, changes in physical quantities over time are explicitly calculated, and a predictor-corrector time integration scheme is used in this study [42]. The position, velocity, and density of the particle are updated in the prediction step as follows:
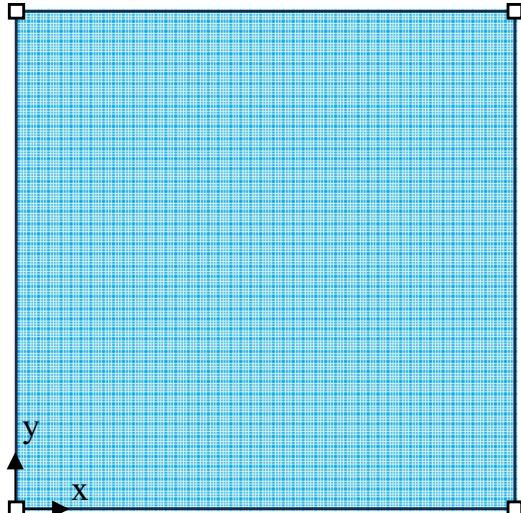
$$
\mathbf{x}_i^{t + \Delta t/2} = \mathbf{x}_i^t + \frac{\Delta t}{2} \mathbf{v}_i^{t + \Delta t/2},
\tag{3.24}
$$

$$
\mathbf{v}_i^{t + \Delta t/2} = \mathbf{v}_i^t + \frac{\Delta t}{2} \left(\frac{D\mathbf{v}_i}{Dt} \right)^t,
\tag{3.25}
$$

$$
\rho_i^{t + \Delta t/2} = \rho_i^t + \frac{\Delta t}{2} \left(\frac{D\rho_i}{Dt} \right)^t,
\tag{3.26}
$$

in which the superscript $t + \Delta t/2$ represents the value predicted in the prediction step. In the correction step, the governing equation is solved based on the physical quantity predicted in the prediction step and the
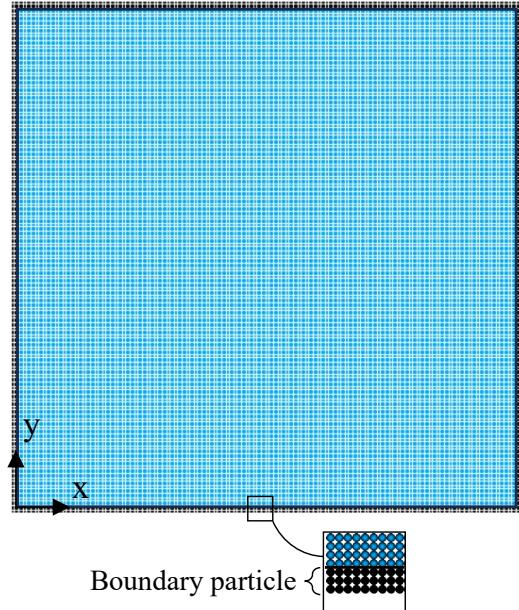
11

Figure 7: Particle discretization domain for natural convection in a square cavity problem using the (a) segment-based boundary treatment method (proposed) and (b) boundary particle method.

value in the next step is determined as follows:

$$\mathbf{x}_i^{t+\Delta t} = \mathbf{x}_i^t + \Delta t \mathbf{v}_i^{t+\Delta t}, \tag{3.27}$$

$$\mathbf{v}_i^{t+\Delta t} = \mathbf{v}_i^t + \Delta t \left(\frac{D\mathbf{v}_i}{Dt}\right)^{t+\Delta t/2}, \tag{3.28}$$

$$\rho_i^{t+\Delta t} = \rho_i^t + \Delta t \left(\frac{D\rho_i}{Dt}\right)^{t+\Delta t/2}, \tag{3.29}$$

in which the superscript $t + \Delta t$ represents the next step.

For numerical stability, the time step size Δt should be determined using the Courant-Friedrichs-Lewy (CFL) condition. In SPH, the CFL condition is given by [43]:

$$\Delta t \leq 0.5 \frac{h}{c + |\mathbf{v}_{\max}|}. \tag{3.30}$$

For all numerical examples in this study, simulations are performed by fixing Δt to satisfy Eq. (3.30).

Table 1: For the SPH results using Boundary particle method, calculation time and particle number ratio compared to the proposed method, and number of boundary segments used in the proposed method.

Problem domain	Square cavity	Horizontal concentric annulus	Complex shaped cavity
Computational time ratio	0.9294	0.85	0.8609
Number of particles ratio	0.9429	0.9226	0.9301
Number of segments	4	60	10

4 Results

In this section, we present three numerical examples to validate the proposed method: natural convection in a square cavity, natural convection in a horizontal concentric annulus, and a complex-shaped cavity. We assess the accuracy and robustness of the proposed method using two benchmark problems that are commonly used to validate numerical simulations of natural convection. Moreover, we demonstrate the versatility of our method by applying it to an example with complex boundary shapes. For all the examples, we verify the proposed method through SPH using boundary particles and FVM, a representative numerical method. For FVM, we use OpenFOAM, a widely used open-source tool. For the boundary particle method, the model proposed in Ref. [16] is used, and three-layered boundary particles are used for all examples.

Table 1 shows the ratio between the calculation times of the proposed method and the boundary particle method for each example. In all three numerical examples, the calculation times of the proposed method are approximately faster 8-15% faster. This shows slightly reduction in computational efficiency compared with the research results using the existing segment-based boundary treatment method [30], and can be attributed to the ratio of the total number of particles used to model the domain. All three numerical examples performed in this study have problem domains in which the fluid particles are fully filled within boundaries. That is, the number of fluid particles is relatively greater than that of boundary particles. In other words, because the total number of particles used in the boundary particle method and the proposed method are not significantly different, the difference in computational efficiency appears to be smaller than reported in previous studies.

4.1 Natural convection in a square cavity

We consider the natural convection in a square cavity as the first numerical example. As shown in Fig. 6, this is an example in which buoyant flow occurs inside a rectangular box owing to the different temperature distributions on both side walls. This example has a very simple geometry, making it easy to define dimensionless coefficients such as the Prandtl and Rayleigh numbers associated with thermo–fluid dynamics. Because of these characteristics, this benchmark problem has been extensively tested as a validation case in various numerical methods.

The length L of one side of the square box is set to 0.1 m. The temperature of the left wall T_{hot} is 300.53487 K, the temperature of the right wall T_{cold} is 299.496513 K, and the temperature difference ΔT ($= T_{hot} - T_{cold}$) between the two walls is 1.006974 K. The initial density of the internal fluid ρ_0 is 1.2 kg/m^3, dynamic viscosity μ is 1.846$\times 10^{-5}$ Pa s, thermal expansion coefficient β is 0.0034 K^{-1}, specific

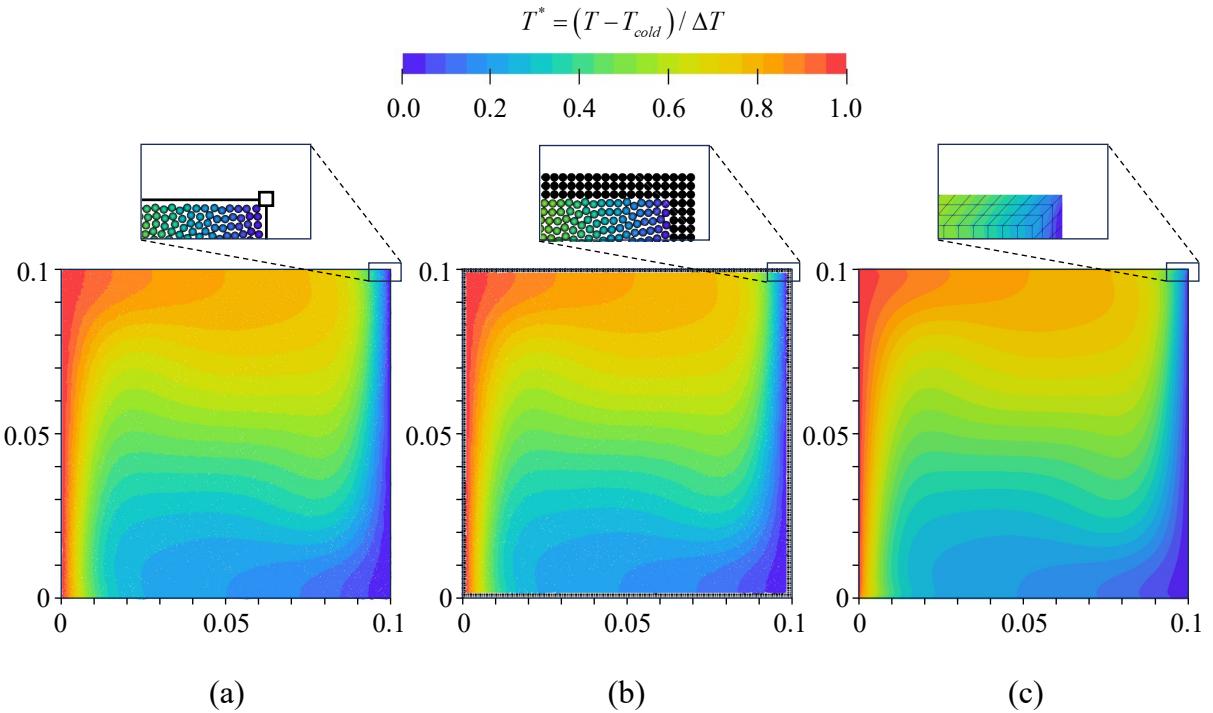$$T^* = \left(T - T_{cold}\right) / \Delta T$$

Figure 8: Comparison of the temperature contours for natural convection in a square cavity problem among three methods: (a) SPH with segment-based boundary treatment method (proposed), (b) SPH with boundary particle method, and (c) FVM.
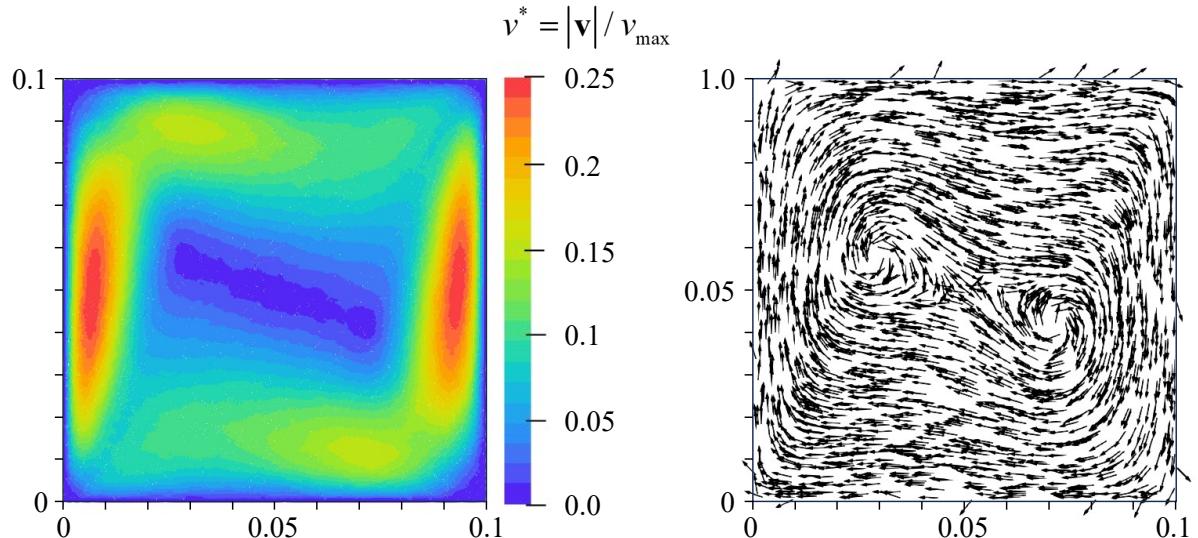
$$v^* = \left|\mathbf{v}\right| / v_{max}$$

Figure 9: Velocity field distribution from the results of the proposed method for natural convection in a square cavity problem: (a) velocity magnitude contour and (b) velocity vector distribution. Note that the velocity vector arrow size is not scaled to its magnitude.

14

Table 2: OpenFOAM setting information. Note that All setting names use the OpenFOAM setting names for the reader's convenience.

Problem domain		Square cavity	Horizontal concentric annulus	Complex shaped cavity
Mean grid size (m)		0.00094	0.00052	0.0047
deltaT (s)		5×10^{-4}	2.5×10^{-4}	0.02
Turbulence model		kOmegaSST		
Wall treatment		kqRWallFunction / omegaWallFunction / nutUWallFunction		
Pressure-velocity coupling		PIMPLE		
fvSchemes	ddtSchemes	Euler		
	gradSchemes	Gaus linear		
	divSchemes	Bounded Gauss limitedLinear		
	laplacianSchemes	Gauss linear orthogonal		
	interpolationSchemes	Linear		
	snGradSchemes	orthogonal		
thermoType	Type	heRhoThermo		
	mixture	pureMixture		
	transport	const		
	Thermo	hConst		
	equationOfState	Boussinesq		
	Specie	specie		
	Energy	sensibleEnthalpy		

heat capacity C_p is 1000 J/(kg K), and thermal conductivity k is 0.0262 W/(m k), the initial temperature distribution T_0 is 300 K, and the gravitational acceleration g is 9.81 m/s^{-2}. In this case, the dimensionless Rayleigh number Ra ($= \rho_0{}^2 C_p g \beta \Delta T L^3/(k\mu)$), which represents the thermal behavior characteristics of the fluid, is 100,000, and the Prandtl number Pr ($= C_p\mu/k$) is 0.7046.

In the SPH simulation, the initial particle spacing Δx is set to confirm the convergence according to particle resolution through three cases of 0.002, 0.001, and 0.0005 m, and the time step size for each case, chosen to satisfies Eq. (3.30), are 2×10^{-3}, 1×10^{-3}, and 5×10^{-4} s, respectively. $v_{\max}$ to calculate the numerical speed of sound c in Eq. (3.10) is calculated as $v_{\max} = \sqrt{g\beta\Delta T L}$. Figs. 7(a) and (b) show the particle discretization domain for the proposed method and boundary particle method, respectively, where Δx= 0.0005 m. For the slip condition, a no-slip boundary condition is imposed to all wall boundaries.

In the FVM simulation, 11200 grids are used to model the problem domain, and the time step size is 5×10^{-4} s. It is simulated using an incompressible transient solver, the turbulence model is k-omega, and the state equation is Boussinesq approximation. The detailed setting information is provided in Table 2.

Fig. 8(a) shows the temperature contour for the Δx= 0.0005 m case at $t = 50$ s. On the left, at the hot wall, a thick layer of fluid with higher temperature forms as the fluid temperature increases with height. On the right, at the cold wall, a thick layer of fluid with lower temperature forms as the fluid temperature decreases with downward movement. As shown in Fig. 9, this temperature distribution induces a buoyancy force in the fluid, resulting in counterclockwise circulation in the outer fluid (closer to the wall). On the
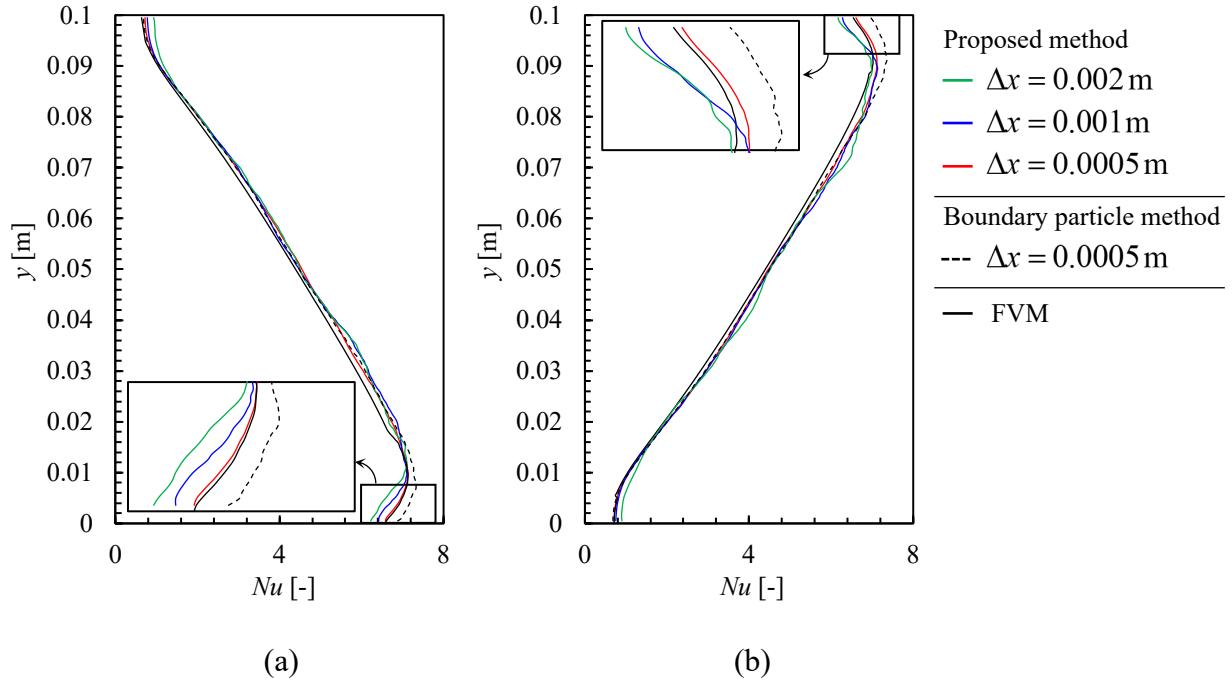
Figure 10: Nu profile comparison among three methods (the proposed method, boundary particle method, and FVM) and convergence test at dx=0.002, 0.001, and 0.0005 m: (a) Nu profile along a hot wall and (b) Nu profile along a cold wall.

other hand, vortices rotating in opposite directions are observed on both sides of the center. Figs. 8(b) and (c) show the results of SPH using boundary particles and FVM, respectively, demonstrating a qualitative alignment with the outcomes of the proposed method.

To verify the accuracy of the proposed method through results of each method, the distribution of Nusselt number Nu $(= -\frac{dT}{dx}\frac{L}{\Delta T})$ is compared quantitatively. Nu is the ratio of the heat transfer by conduction to that by convection at the boundary surface. The distributions of Nu on both sides of the wall are compared. Figs. 10(a) and (b) show the comparisons of the three methods for the hot and cold walls, respectively. The quantitative results of the proposed method tend to be in good agreement with the results of SPH using the boundary particles and FVM. In addition, the convergence of the proposed method is confirmed to be closer to the FVM results, as the particle resolution becomes finer.

4.2 Natural convection in a horizontal concentric annulus

We consider the natural convection in a horizontal concentric annulus, shown in Fig. 11, as the second numerical example. Natural convection occurs owing to the temperature difference between the inner and the outer cylinders. This example allows us verify the numerical analysis results against the experiments performed by [44]. That is, the proposed method is validated by comparison with experimental results as well as other numerical approaches such as FVM and SPH with boundary particles.

The radius R_{inner} and temperature T_{hot} of the inner circle are 0.02 m and 323.664 K, respectively. the radius R_{outer} and temperature T_{cold} of the outer circle are 0.052 m and 300 K, respectively. The temperature
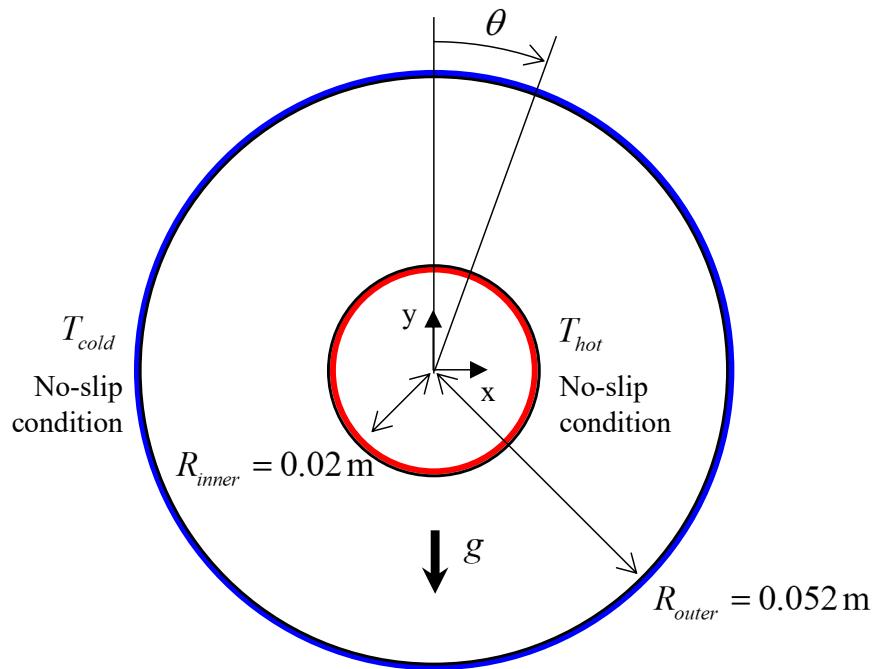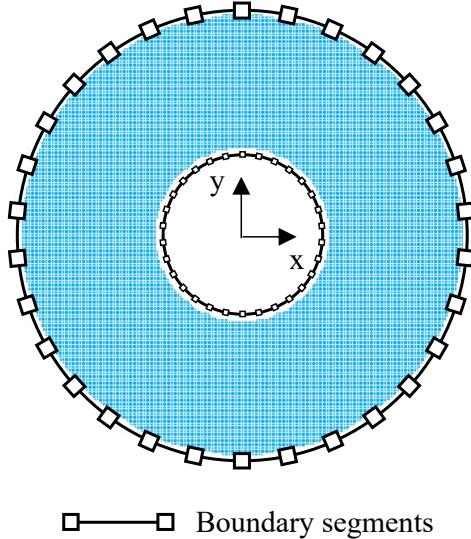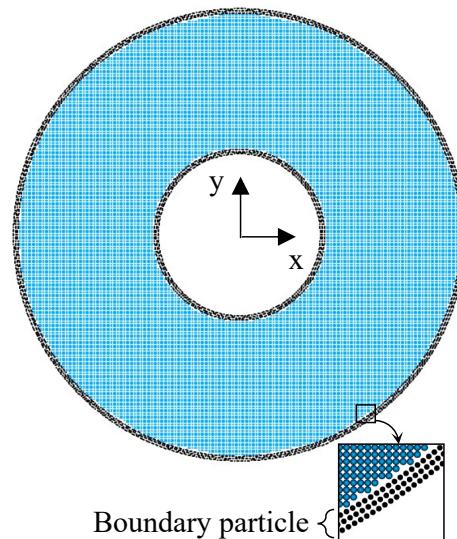
16

Figure 11: Domain description for natural convection in a horizontal concentric annulus problem.

Segment based boundary method　　Boundary particle method

□———□ Boundary segments　　Boundary particle {

(a)　　　　　　　　　　　　　　(b)

Figure 12: Particle discretization domain for natural convection in a horizontal concentric annulus problem using (a) segment-based boundary treatment method (proposed) and (b) boundary particle method.
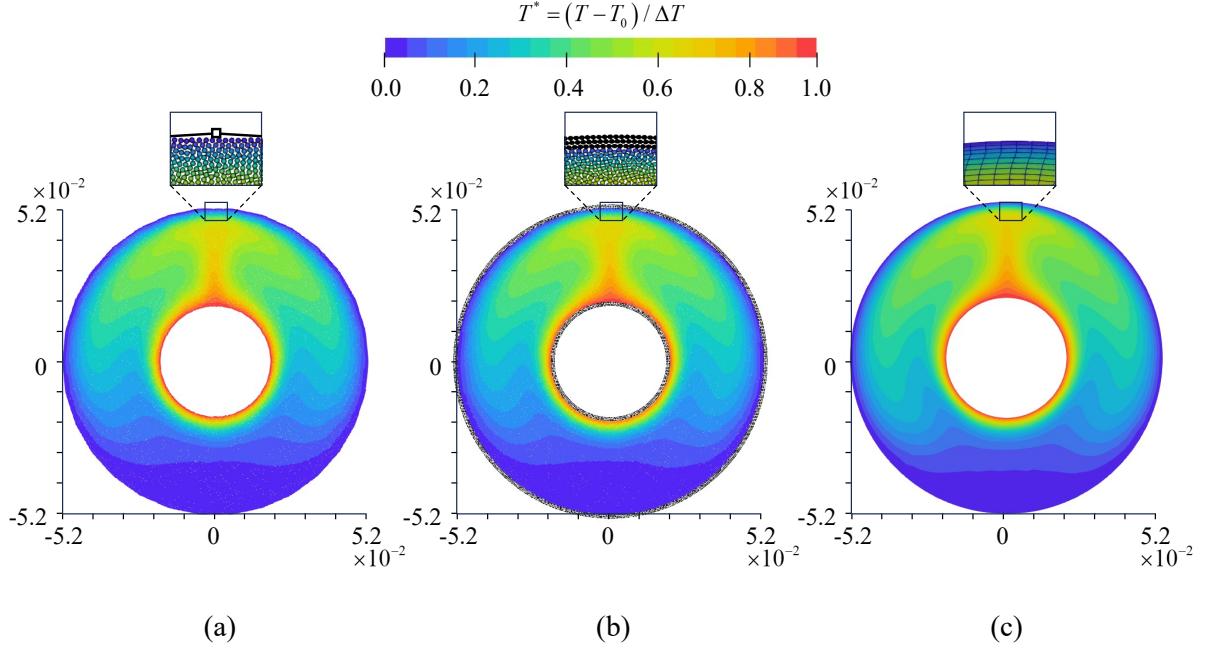
Figure 13: Comparison of the temperature contours for natural convection in a horizontal concentric annulus problem among three methods: (a) SPH with segment-based boundary treatment method (proposed), (b) SPH with boundary particle method, and (c) FVM.

difference ΔT between the inner and outer circles is 23.664 K. The initial density of the internal fluid ρ_0 is 1.096 kg/m^3, dynamic viscosity μ is 2.0×10^{-5} Pa s, thermal expansion coefficient β is 0.003 K^{-1}, specific heat capacity C_p is 1006.3 J/(kg K), and thermal conductivity k is 0.02816 W/(m k), the initial temperature distribution T_0 is 300 K, and the gravitational acceleration g is 9.81 m/s^{-2}. In this case, the dimensionless Rayleigh number Ra ($= \rho_0{}^2 C_p g \beta \Delta T (R_{outer} - R_{inner})^3/(k\mu)$), which represents the thermal behavior characteristics of the fluid, is 4.9×10^4 and the Prandtl number Pr is 0.7147.

In the SPH simulation, the initial particle spacing Δx is set to verify convergence according to particle resolution for the three cases of 0.002, 0.001, and 0.0005 m. The time step size Δt for each case is set to 1×10^{-3}, 5×10^{-4}, and 2.5×10^{-4} s, respectively. $v_{\max}$ is calculated as $v_{\max} = \sqrt{g\beta\Delta T(R_{outer} - R_{inner})}$ and uses a value of 0.15. Figs. 12(a) and (b) show the particle discretization domain for the proposed method and the method using boundary particles, respectively. Here, Δx is 0.0005 m. For the slip condition, a no-slip boundary condition is imposed on all wall boundaries.

In the FVM simulation, 26580 grids are used to model the problem domain, and the time step size is 2.5x10-4 s. It is simulated using an incompressible transient solver, the turbulence model is k-omega, and the state equation is the Boussinesq approximation. The detailed setting information is provided in Table 2.

Fig. 13(a) illustrates the temperature contour of the proposed method for the case where Δx is 0.0005 m at t= 20 s. The heat of the fluid adjacent to the inner hot wall gradually transfers outward, resulting in buoyancy owing to the temperature difference. As shown in Fig. 14, the fluid particles heated by the inner cylinder rise, cool upon reaching the outer cylinder, and then descend along the outer perimeter, creating an overall circulation. As shown in Figs. 13(a)-(c), the results of the proposed method exhibit a favorable
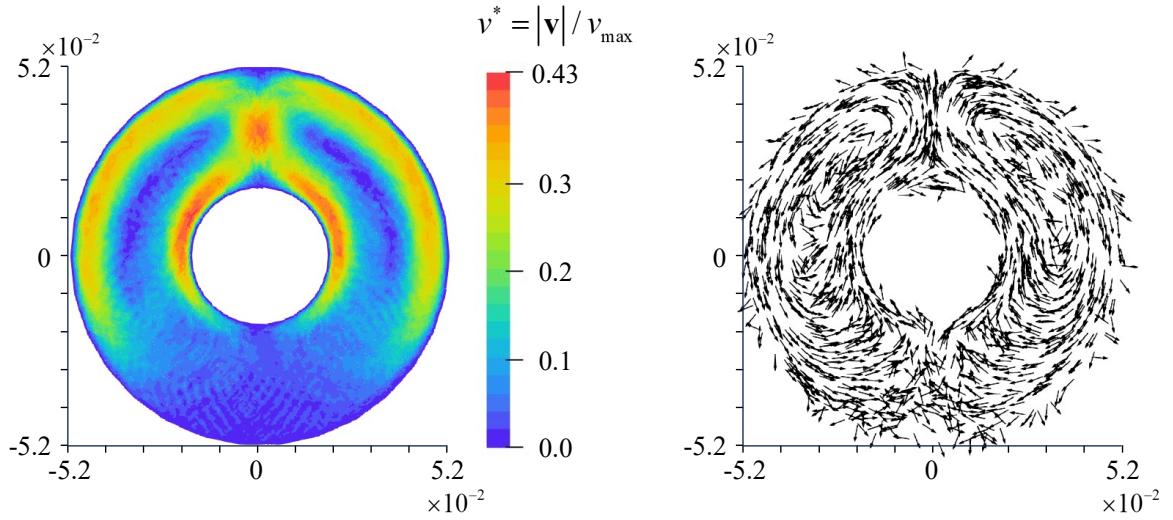
18

Figure 14: Velocity field distribution from the results of the proposed method for natural convection in a horizontal concentric annulus problem: (a) velocity magnitude contour and (b) velocity vector distribution. Note that the velocity vector arrow size is not scaled to its magnitude.
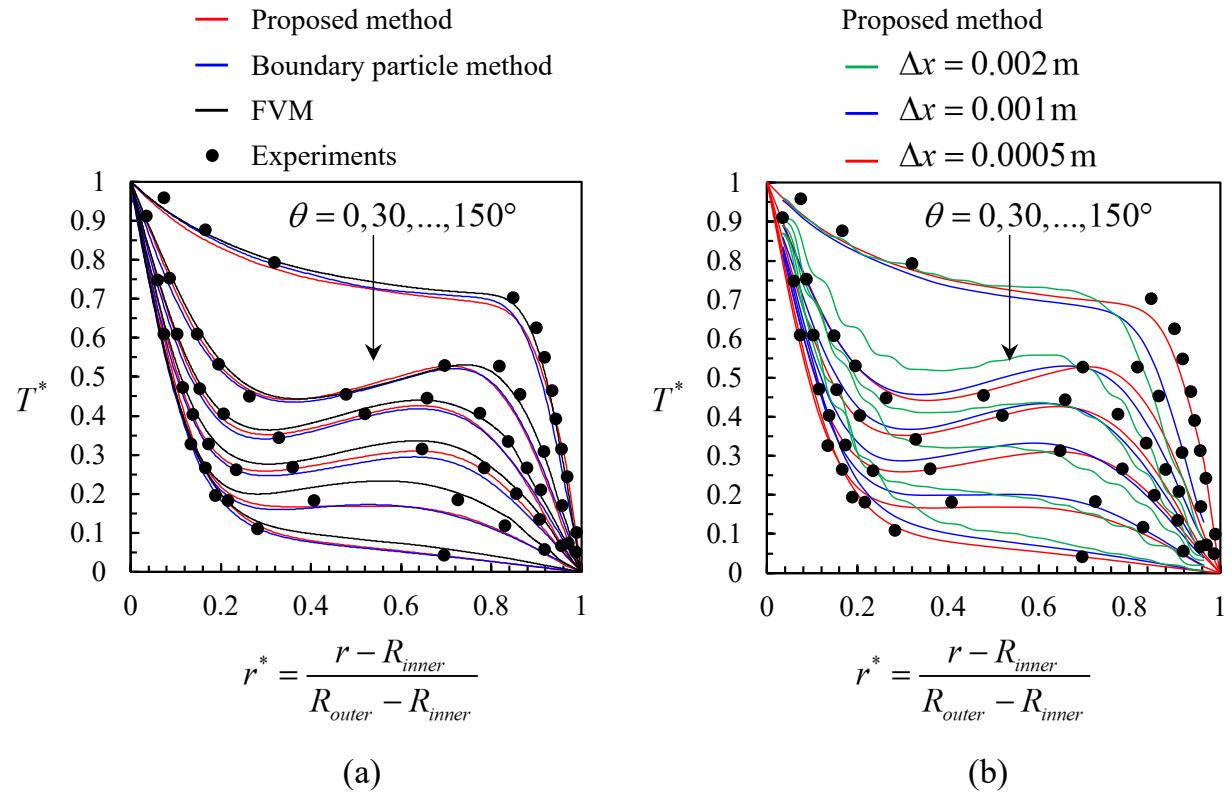

Figure 15: Non-dimensionalized temperature profile on different θ lines: (a) comparison between the proposed method, boundary particle method, FVM and experiments, and (b) convergence test at dx=0.002, 0.001, and 0.0005 m.

19
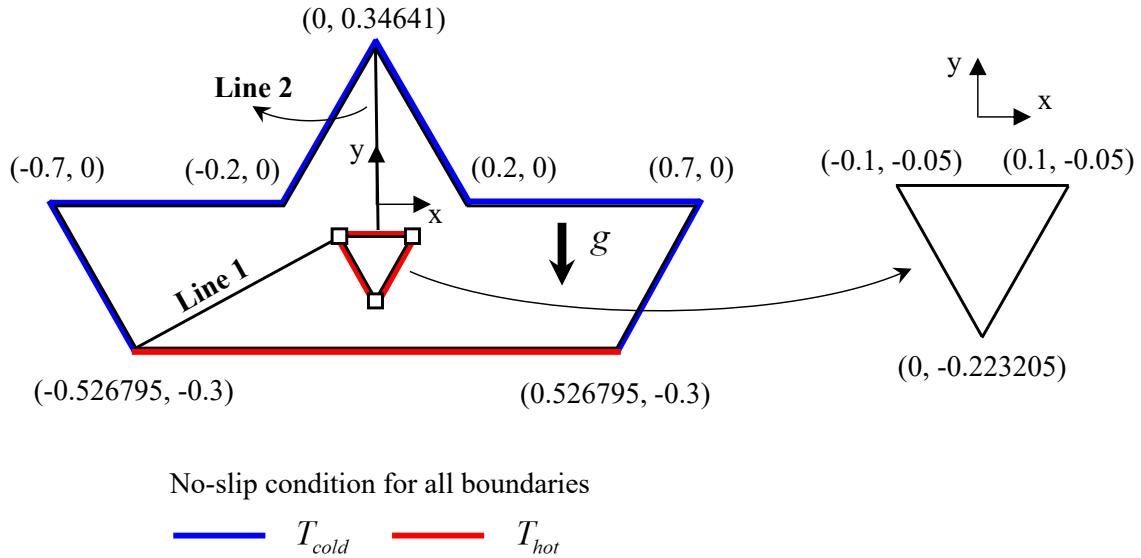
Figure 16: Domain description for a complex shaped cavity problem.

alignment with the SPH results using boundary particles and FVM simulations.

For this benchmark problem, the results can be quantitatively verified using the experimental data from [44]. In the problem domain description in Fig. 11, the θ value is increased by 30 °, and the non-dimensionalized temperature T* is measured as $(T - T_{cold})/\Delta T$. Fig. 15(a) compares the proposed method with the boundary particle method, FVM, and experimental results, revealing good agreement. Fig. 15(b) shows the results of the convergence test. The proposed method shows a tendency to agree well with the results obtained using the boundary particle method, FVM, and experiments. In the convergence test, the oscillation of the temperature profile is observed when $\Delta x = 0.002$ m. In SPH, the temperature at the probe point is obtained by referring to the temperature values of surrounding particles [45]. A coarse particle resolution can lead to large temperature differences among the referenced particles at the probe point, resulting in oscillations.

4.3   Complex shaped cavity

As a final example, a flow analysis is performed in a cavity with a complex shape, as shown in Fig. 16. The proposed method offers greater modeling flexibility than the boundary particle method. While modelling complex shapes is relatively easy, demonstrating that the solution remains accurate and stable for such complexities is eqactically important. To account for the influence of the geometrc complexity, the flow distribution must exhibit stability at both concave and convex corners. As shown in Fig. 17, the shape is designed such that the angles formed between the line segments are distributed across all four quadrants of the angle graph. The simulation results are verified by comparison with the FVM results.

The domain consists of outer boundary and inner boundaries. The outer boundary consists of the following seven nodes: (0, 0.34641), (-0.2, 0), (-0.7, 0), (-0.526795, -0.3), (0.526795, -0.3), (0.7, 0), and (0.2, 0). The internal boundary consists of the following 3 nodes: (-0.1, -0.05), (0.1, -0.05), and (0, -0.223205),
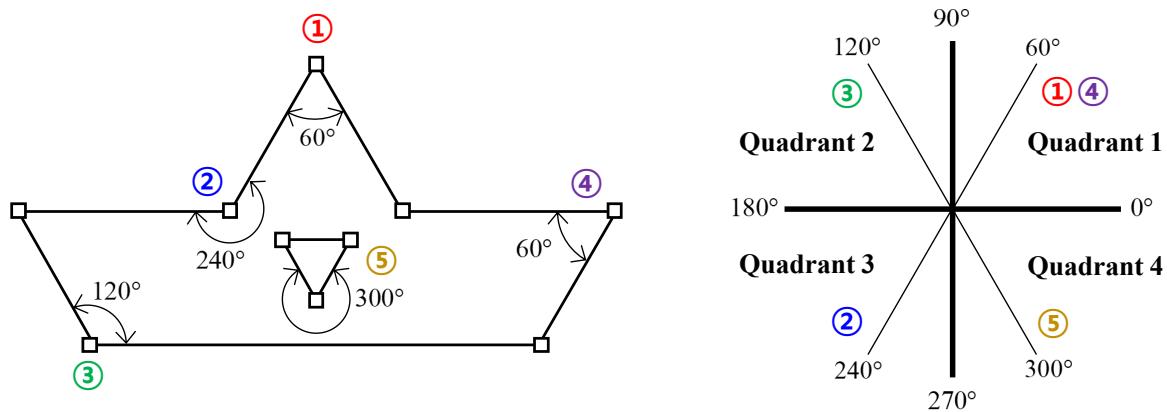
Figure 17: Angle distribution between boundary segments for a complex shaped cavity problem.

Segment based boundary method
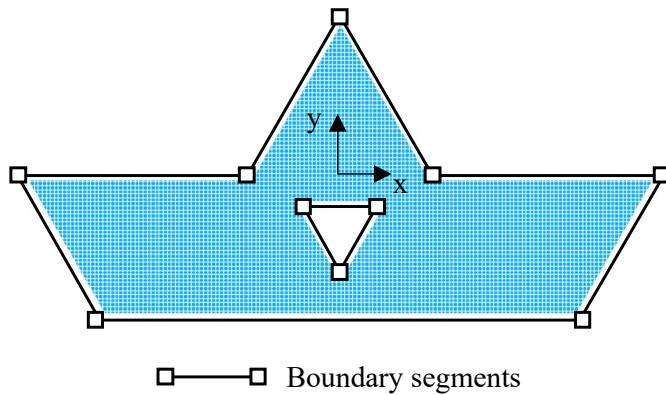

□———□ Boundary segments

Figure 18: Particle discretization domain for a complex shaped cavity problem using segment-based boundary treatment method.
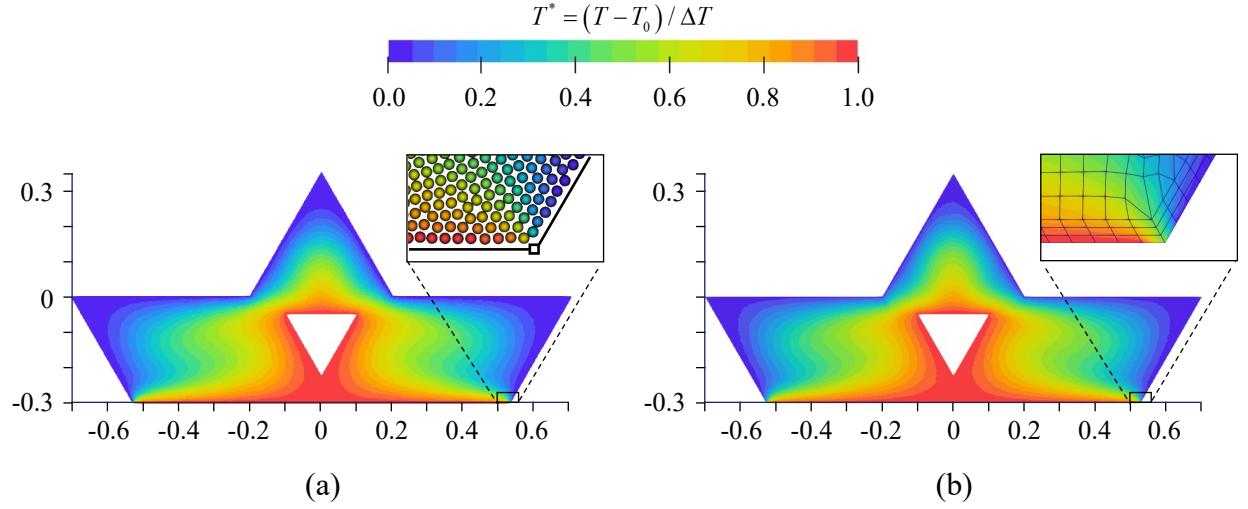
Figure 19: Comparison of the temperature contours for complex shaped cavity problem between two methods: (a) SPH with segment-based boundary treatment method (proposed) and (b) FVM.
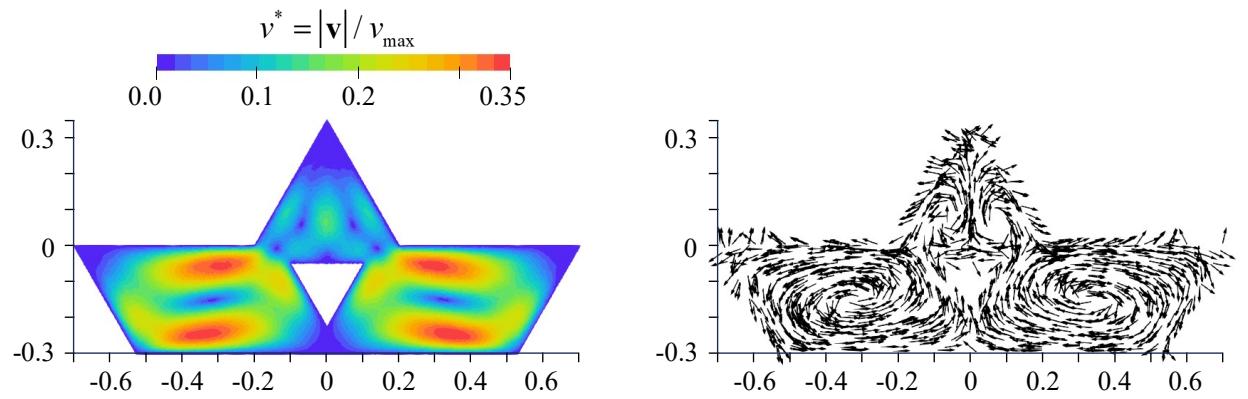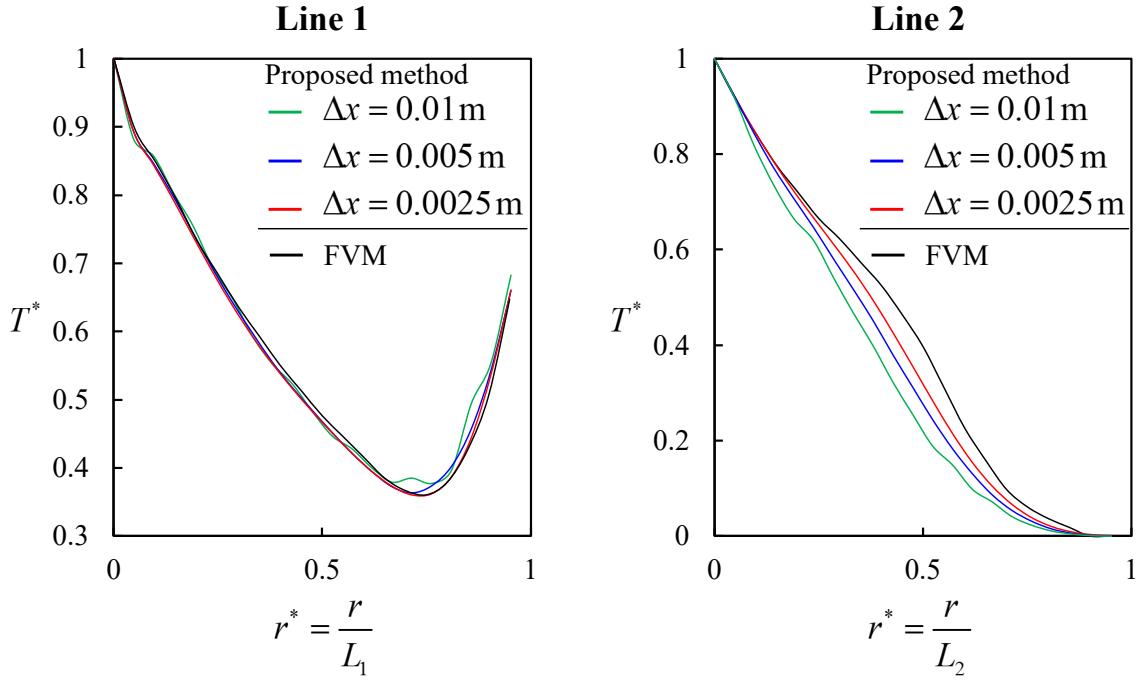

Figure 20: Velocity field distribution from the results of the proposed method for a complex shaped cavity problem: (a) velocity magnitude contour and (b) velocity vector distribution. Note that the velocity vector arrow size is not scaled to its magnitude.

Line 1

Line 2

Figure 21: Comparison of the non-dimensionalized temperature profiles between the proposed method and FVM, and convergence tests at dx=0.01, 0.005, and 0.0025 m: (a) results along line1 and (b) results along line2.

see Fig. 16. The unit for all node positions is meters. The temperature of the outer boundary, excluding the bottom wall, is 300.0 K, while that of the bottom wall is 300.005 K. The temperature of the inner boundary is set to 300.005 K, so that the maximum temperature difference between the boundaries is ΔT= 0.005 K. The initial density of the internal fluid ρ_0 is 1.0 kg/ m^3, dynamic viscosity μ is 2.0×10^{-5} Pa s, thermal expansion coefficient β is 0.003 K^{-1}, specific heat capacity C_p is 1000 J/(kg K), thermal conductivity k is 0.028 W/(m k), the initial temperature distribution T_0 is 300 K, and the gravitational acceleration g is 9.81 m/s^{-2}. The reference length L_{ref} to define $v_{\max}$ is set to 0.3 m. In this case Ra is 7.1×10^3 and Pr is 0.7143.

In the SPH simulation, three cases, with initial particle spacings Δx of 0.01, 0.005, and 0.0025 m, are considered, and the time step sizes Δt for each case are set to 0.1, 0.05, and 0.02 s, respectively. $v_{\max}$ is calculated as $v_{\max} = \sqrt{g\beta\Delta T L_{ref}}$ and is 0.0066 m/s. Fig. 18 shows the particle discretization domain for the proposed method when Δx= 0.0025 m. For the slip condition, a no-slip boundary condition is imposed on all wall boundaries.

In the FVM simulation, 18994 grids are used to model the problem domain, and the time step size is 0.02 s. It is simulated using an incompressible transient solver, the turbulence model is k-omega, and the state equation is the Boussinesq approximation. The detailed setting information is provided in Table 2.

Fig. 19(a) shows the temperature contour of the proposed method for the Δx= 0.0025 m case at t= 1000 s. Buoyancy occurs depending on the temperature difference between each wall, which causes the circulation of internal flow (Fig. 20). The results of the proposed method match well with the FVM results, as shown in Figs. 19(a) and (b).

To examine the accuracy of the proposed method, a comparison with FVM is performed on the temper-

ature distribution along the two lines with the largest thermal change rate in the domain. Line 1 is defined by the following two positions: (-0.1, -0.05) and (-0.526795, -0.3). Line 2 is defined by the following two positions: (0, -0.05) and (0, 0.34641), see Fig. 16. Here, the unit of position is meters. In Fig. 21, the results of the two methods (the proposed method and FVM) are in good agreement, and the proposed method accurately simulates heat transfer from the wall boundary to the internal fluid. Note that the r is the distance from each line's initial position to end position, and L_1 and L_2 denote the lengths of line 1 and line 2, respectively.

5 Conclusion

In this study, we proposed an SPH model to simulate the natural convection induced by heat transfer from wall boundaries. Traditionally, SPH mainly uses multi-layer boundary particles for wall boundary modeling, but this has limitations such as complexities in boundary modeling and increased computational cost. To solve this issues, the segment-based boundary treatment method has recently attracted attention. This study aimed to develop a wall heat transfer model based on this method.

In SPH, wall boundary modeling through segments was performed using lines in 2D and faces in 3D, offering the advantage of easy applicability, even for complex boundary shapes. Unlike the boundary particle method, which requires the entire boundary modeling with a resolution equivalent to the fluid particle size even for simple shapes, the segment-based approach only requires the modeling of segments where the normal vector of the boundary shape differs, leading to reduced computational costs. The model was derived through a mathematically rigorous derivation process, to maintain accuracy when using segments instead of boundary particles. The validity of the proposed method was confirmed through a comparison with the available experimental results, results obtained using boundary particles in SPH, and results from FVM.

SPH is widely used in the industry and academia because of its unique characteristics. However, there is substantial room for further development in terms of accuracy and practicality. The methodology presented in this paper holds the potential for practical application in a broader array of problems. A limitation of this study is the need to explore more diverse boundary conditions, such as the moving boundary and Neumann boundary conditions. In future work, we aim to overcome these limitations and extend the proposed method to three-dimensions for extensive applications.

Declaration of competing interest

The authors declare that they have no known competing financial interests or personal relationships that could have appeared to influence the work reported in this paper.

Acknowledgement

References

[1] M. Schaub, M. Kriegel, and S. Brandt. "Experimental Investigation of Heat Transfer by Unsteady Natural Convection at a Vertical Flat Plate". In: *International Journal of Heat and Mass Transfer* 136 (June 2019), pp. 1186–1198. ISSN: 0017-9310. DOI: 10.1016/j.ijheatmasstransfer.2019.03.089. (Visited on 10/28/2023).

[2] M.-H. Kim and H.-J. Park. "Application of Artificial Neural Networks Using Sequential Prediction Approach in Indoor Airflow Prediction". In: *Journal of Building Engineering* 69 (2023), p. 106319. DOI: 10.1016/j.jobe.2023.106319.

[3] Y. Zhao and B. Zhang. "A High-Order Characteristics Upwind FV Method for Incompressible Flow and Heat Transfer Simulation on Unstructured Grids". In: *Computer Methods in Applied Mechanics and Engineering* 190.5 (Nov. 2000), pp. 733–756. ISSN: 0045-7825. DOI: 10.1016/S0045-7825(99)00443-0. (Visited on 10/28/2023).

[4] A.-N. Eiyad. "Effects of Variable Viscosity and Thermal Conductivity of Al2O3–Water Nanofluid on Heat Transfer Enhancement in Natural Convection". In: *International Journal of Heat and Fluid Flow* 30.4 (Aug. 2009), pp. 679–690. ISSN: 0142-727X. DOI: 10.1016/j.ijheatfluidflow.2009.02.003. (Visited on 10/28/2023).

[5] H.-J. Kim et al. "A multi-director continuum beam finite element for efficient analysis of multi-layer strand cables". In: *Computers & Structures* 256 (2021), p. 106621.

[6] J. Kim and J. D. Park. "The Non-Homogeneous Flow of a Thixotropic Fluid around a Sphere". In: *Applied Mathematical Modelling* 82 (2020), pp. 848–866. DOI: 10.1016/j.apm.2020.02.009.

[7] J. Kim. "Adjoint-Based Sensitivity Analysis of Viscoelastic Fluids at a Low Deborah Number". In: *Applied Mathematical Modelling* 115 (2023), pp. 453–469. DOI: 10.1016/j.apm.2022.10.044.

[8] B. Zhao and Z. Tian. "High-Resolution High-Order Upwind Compact Scheme-Based Numerical Computation of Natural Convection Flows in a Square Cavity". In: *International Journal of Heat and Mass Transfer* 98 (July 2016), pp. 313–328. ISSN: 0017-9310. DOI: 10.1016/j.ijheatmasstransfer.2016.03.032. (Visited on 10/28/2023).

[9] R. Kumar and A. Dewan. "A Study of LES–SGS Closure Models Applied to a Square Buoyant Cavity". In: *International Journal of Heat and Mass Transfer* 98 (July 2016), pp. 164–175. ISSN: 0017-9310. DOI: 10.1016/j.ijheatmasstransfer.2016.02.057. (Visited on 10/28/2023).

[10] J. J. Monaghan. "Simulating Free Surface Flows with SPH". In: *Journal of computational physics* 110.2 (1994), pp. 399–406. DOI: 10.1006/jcph.1994.1034.

[11] F. P. Bakti et al. "Comparative Study of Standard WC-SPH and MPS Solvers for Free Surface Academic Problems". In: *International Journal of Offshore and Polar Engineering* 26.03 (Sept. 2016), pp. 235–243. ISSN: 1053-5381. DOI: 10.17736/ijope.2016.pf17.

[12] T. Hu et al. "Numerical Simulations of Sloshing Flows with an Elastic Baffle Using a SPH-SPIM Coupled Method". In: *Applied Ocean Research* 93 (Dec. 2019), p. 101950. ISSN: 0141-1187. DOI: `10.1016/j.apor.2019.101950`. (Visited on 10/30/2023).

[13] G.-R. Liu and M. B. Liu. *Smoothed Particle Hydrodynamics: A Meshfree Particle Method*. World scientific, 2003.

[14] M. B. Liu et al. "Smoothed Particle Hydrodynamics for Numerical Simulation of Underwater Explosion". In: *Computational Mechanics* 30.2 (Jan. 2003), pp. 106–118. ISSN: 1432-0924. DOI: `10.1007/s00466-002-0371-6`. (Visited on 10/30/2023).

[15] M. B. Liu and G. R. Liu. "Smoothed Particle Hydrodynamics (SPH): An Overview and Recent Developments". In: *Archives of Computational Methods in Engineering* 17.1 (Mar. 2010), pp. 25–76. ISSN: 1886-1784. DOI: `10.1007/s11831-010-9040-7`. (Visited on 10/30/2023).

[16] M. Liu, J. R. Shao, and J. Z. Chang. "On the Treatment of Solid Boundary in Smoothed Particle Hydrodynamics". In: *Science China Technological Sciences* 55 (2012), pp. 244–254. DOI: `10.1007/s11431-011-4663-y`.

[17] P. W. Cleary. "Modelling Confined Multi-Material Heat and Mass Flows Using SPH". In: *Applied Mathematical Modelling* 22.12 (Dec. 1998), pp. 981–993. ISSN: 0307-904X. DOI: `10.1016/S0307-904X(98)10031-8`. (Visited on 10/26/2023).

[18] K. Szewc, P. J., and A. Tanière. "Modeling of Natural Convection with Smoothed Particle Hydrodynamics: Non-Boussinesq Formulation". In: *International Journal of Heat and Mass Transfer* 54.23 (Nov. 2011), pp. 4807–4816. ISSN: 0017-9310. DOI: `10.1016/j.ijheatmasstransfer.2011.06.034`. (Visited on 10/26/2023).

[19] X. Yang and S.-C. Kong. "Numerical Study of Natural Convection in a Horizontal Concentric Annulus Using Smoothed Particle Hydrodynamics". In: *Engineering Analysis with Boundary Elements* 102 (May 2019), pp. 11–20. ISSN: 0955-7997. DOI: `10.1016/j.enganabound.2019.02.007`. (Visited on 10/14/2023).

[20] K. C. Ng et al. "Assessment of Smoothed Particle Hydrodynamics (SPH) Models for Predicting Wall Heat Transfer Rate at Complex Boundary". In: *Engineering Analysis with Boundary Elements* 111 (Feb. 2020), pp. 195–205. ISSN: 09557997. DOI: `10.1016/j.enganabound.2019.10.017`. (Visited on 08/21/2023).

[21] F. Garoosi and A. Shakibaeinia. "An Improved High-Order ISPH Method for Simulation of Free-Surface Flows and Convection Heat Transfer". In: *Powder Technology* 376 (Oct. 2020), pp. 668–696. ISSN: 0032-5910. DOI: `10.1016/j.powtec.2020.08.074`. (Visited on 10/25/2023).

[22] P. Yang et al. "Simulating Natural Convection with High Rayleigh Numbers Using the Smoothed Particle Hydrodynamics Method". In: *International Journal of Heat and Mass Transfer* 166 (Feb. 2021), p. 120758. ISSN: 0017-9310. DOI: `10.1016/j.ijheatmasstransfer.2020.120758`. (Visited on 10/01/2023).

[23] J. Bonet and T.-S.L. Lok. "Variational and Momentum Preservation Aspects of Smooth Particle Hydrodynamic Formulations". In: *Computer Methods in Applied Mechanics and Engineering* 180.1-2 (1999), pp. 97–115. ISSN: 00457825. DOI: 10.1016/S0045-7825(99)00051-1. (Visited on 09/07/2023).

[24] J. Feldman and J.Bonet. "Dynamic Refinement and Boundary Contact Forces in SPH with Applications in Fluid Flow Problems". In: *International Journal for Numerical Methods in Engineering* 72.3 (2007), pp. 295–324. DOI: 10.1002/nme.2010.

[25] A. Leroy et al. "Unified Semi-Analytical Wall Boundary Conditions Applied to 2-D Incompressible SPH". In: *Journal of Computational Physics* 261 (2014), pp. 106–129. DOI: 10.1016/j.jcp.2013.12.035.

[26] Sivakumar Kulasegaram et al. "A Variational Formulation Based Contact Algorithm for Rigid Boundaries in Two-Dimensional SPH Applications". In: *Computational Mechanics* 33 (2004), pp. 316–325. DOI: 10.1007/s00466-003-0534-0.

[27] M. Ferrand et al. "Unified Semi-Analytical Wall Boundary Conditions for Inviscid, Laminar or Turbulent Flows in the Meshless SPH Method". In: *International Journal for Numerical Methods in Fluids* 71.4 (2013), pp. 446–472. DOI: 10.1002/fld.3666.

[28] A. Mayrhofer et al. "Unified Semi-Analytical Wall Boundary Conditions in SPH: Analytical Extension to 3-D". In: *Numerical Algorithms* 68 (2015), pp. 15–34. DOI: 10.1007/s11075-014-9835-y.

[29] W. Kostorz and A. Esmail-Yakas. "Semi-Analytical Smoothed-Particle Hydrodynamics Correction Factors for Polynomial Kernels and Piecewise-Planar Boundaries". In: *International Journal for Numerical Methods in Engineering* 122.24 (2021), pp. 7271–7305. DOI: 10.1002/nme.6771.

[30] H.-J. Park, H.-D. Seo, and P.-S. Lee. "Direct Imposition of the Wall Boundary Condition for Simulating Free Surface Flows in SPH". In: *Structural Engineering and Mechanics, An Int'l Journal* 78.4 (2021), pp. 497–518. DOI: 10.12989/sem.2021.78.4.497.

[31] R. J. Singh and T. B. Gohil. "Numerical Analysis of Unsteady Natural Convection Flow and Heat Transfer in the Existence of Lorentz Force in Suddenly Expanded Cavity Using Open FOAM". In: *Journal of Thermal Science* 29.6 (Nov. 2020), pp. 1513–1530. ISSN: 1993-033X. DOI: 10.1007/s11630-020-1190-9. (Visited on 10/30/2023).

[32] J. Wang et al. "Modeling Heat Transfer Subject to Inhomogeneous Neumann Boundary Conditions by Smoothed Particle Hydrodynamics and Peridynamics". In: *International Journal of Heat and Mass Transfer* 139 (Aug. 2019), pp. 948–962. ISSN: 0017-9310. DOI: 10.1016/j.ijheatmasstransfer.2019.05.054. (Visited on 10/01/2023).

[33] X. Y. Hu and N. A. Adams. "An Incompressible Multi-Phase SPH Method". In: *Journal of computational physics* 227.1 (2007), pp. 264–278. DOI: 10.1016/j.jcp.2007.07.013.

[34] J. P. Morris, P. J. Fox, and Y. Zhu. "Modeling Low Reynolds Number Incompressible Flows Using SPH". In: *Journal of computational physics* 136.1 (1997), pp. 214–226. DOI: `10.1006/jcph.1997.5776`.

[35] P. N. Sun et al. "The δplus-SPH Model: Simple Procedures for a Further Improvement of the SPH Scheme". In: *Computer Methods in Applied Mechanics and Engineering* 315 (2017), pp. 25–49. DOI: `10.1016/j.cma.2016.10.028`.

[36] S. Marrone et al. "δ-SPH Model for Simulating Violent Impact Flows". In: *Computer Methods in Applied Mechanics and Engineering* 200.13-16 (2011), pp. 1526–1542. DOI: `10.1016/j.cma.2010.12.016`.

[37] A. Zhang, P. Sun, and F. Ming. "An SPH Modeling of Bubble Rising and Coalescing in Three Dimensions". In: *Computer Methods in Applied Mechanics and Engineering* 294 (2015), pp. 189–209. DOI: `10.1016/j.cma.2015.05.014`.

[38] H.-J. Park and H.-D. Seo. "A New SPH-FEM Coupling Method for Fluid–Structure Interaction Using Segment-Based Interface Treatment". In: *Engineering with Computers* (June 2023). ISSN: 1435-5663. DOI: `10.1007/s00366-023-01856-1`. (Visited on 08/19/2023).

[39] S. Adami, X. Y. Hu, and N. A. Adams. "A Generalized Wall Boundary Condition for Smoothed Particle Hydrodynamics". In: *Journal of Computational Physics* 231.21 (2012), pp. 7057–7075. ISSN: 0021-9991. DOI: `10.1016/j.jcp.2012.05.005`. (Visited on 10/30/2023).

[40] X. Y. Hu and N. A. Adams. "A Multi-Phase SPH Method for Macroscopic and Mesoscopic Flows". In: *Journal of Computational Physics* 213.2 (2006), pp. 844–861. DOI: `10.1016/j.jcp.2005.09.001`.

[41] S. J. Lind et al. "Incompressible Smoothed Particle Hydrodynamics for Free-Surface Flows: A Generalised Diffusion-Based Algorithm for Stability and Validations for Impulsive Flows and Propagating Waves". In: *Journal of Computational Physics* 231.4 (Feb. 2012), pp. 1499–1523. ISSN: 00219991. DOI: `10.1016/j.jcp.2011.10.027`. (Visited on 08/19/2023).

[42] J. J. Monaghan. "On the Problem of Penetration in Particle Methods". In: *Journal of Computational physics* 82.1 (1989), pp. 1–15. DOI: `10.1016/0021-9991(89)90032-6`.

[43] De M. Carlos, A. Kubrusly, and S. Carlos. "The Courant–Friedrichs–Lewy (Cfl) Condition". In: *AMC* 10.12 (2013).

[44] T. H. Kuehn and R. J. Goldstein. "An Experimental Study of Natural Convection Heat Transfer in Concentric and Eccentric Horizontal Cylindrical Annuli". In: *Journal of Heat Transfer* 100.4 (Nov. 1978), pp. 635–640. ISSN: 0022-1481. DOI: `10.1115/1.3450869`. (Visited on 10/14/2023).

[45] A. English et al. "Modified Dynamic Boundary Conditions (mDBC) for General-Purpose Smoothed Particle Hydrodynamics (SPH): Application to Tank Sloshing, Dam Break and Fish Pass Problems". In: *Computational Particle Mechanics* 9.5 (Sept. 2022), pp. 1–15. ISSN: 2196-4386. DOI: `10.1007/s40571-021-00403-3`. (Visited on 10/30/2023).